

# Inversion of magnetic measurements of the *CHAMP* satellite over the Pannonian Basin

K I Kis<sup>a,\*</sup>, P T Taylor<sup>b</sup>, G Wittmann<sup>c</sup>, B Toronyi<sup>d</sup>, S Pusztai<sup>e</sup>

<sup>a</sup>Geophysics and Space Sciences Department Loránd Eötvös University, Pázmány Péter sétány 1/c., 1117 Budapest, Hungary

<sup>b</sup>Planetary Geodynamics Laboratory NASA/GFSC, Greenbelt, MD 20771, USA

<sup>c</sup>MOL Hungarian Oil and Gas Co., Budafoki út 79, 1117 Budapest, Hungary

<sup>d</sup>Institute of Geodesy, Cartography and Remote Sensing, Bosnyák tér 5., 1149 Budapest, Hungary

<sup>e</sup>Geodetic and Geophysical Research Institute Earthquake Observatory, Meredek u. 18., 1112 Budapest, Hungary

\*Corresponding author. Fax.: +36-1-381-2192

*E-mail address:* kisk@ludens.elte.hu

## Abstract

The Pannonian Basin is a deep intra-continental basin that formed as part of the Alpine orogeny. In order to study the nature of the crustal basement we used the long-wavelength magnetic anomalies acquired by the *CHAMP* satellite. The anomalies were distributed in a spherical shell, some 107,927 data recorded between January 1 and December 31 of 2008. They covered the Pannonian Basin and its vicinity. These anomaly data were interpolated into a spherical grid of  $0.5^\circ \times 0.5^\circ$ , at the elevation of 324 km by the Gaussian weight function. The vertical gradient of these total magnetic anomalies was also computed and mapped to the surface of a sphere at 324 km elevation. The former spherical anomaly data at 425 km altitude were downward continued to 324 km. To interpret these data at the elevation of 324 km we used an inversion method. A polygonal prism forward model was used for the inversion. The minimum problem was solved numerically by the Simplex and Simulated annealing methods; a  $L_2$  norm in the case of Gaussian distribution parameters and a  $L_1$  norm was used in the case of Laplace distribution parameters. We INTERPRET THAT the magnetic anomaly WAS produced by several sources and the effect of the stable magnetization of the exsolution of hemo-ilmenite minerals in the upper crustal metamorphic rocks.

*Keywords:* *CHAMP*, Pannonian Basin, total and vertical gradient magnetic anomalies, downward continuation, inversion

## 1. Introduction

The Pannonian Basin extends some 800 by 500 km in a generally east-northeast direction with depths extending to 7 km. Large crustal features produce long wavelength

42 magnetic anomalies. These anomalies are sufficiently resolved by satellite altitude  
43 observations. The German satellite *CHAMP* was launched on July 15, 2000 (Reigber et al.  
44 2003, 2005) and it finished its mission on September 19, 2010. This satellite measured the  
45 gravity and magnetic field of the Earth with high accuracy. The total magnetic data are  
46 obtained by a scalar Overhauser magnetometer developed by the Laboratoire d'Electronique  
47 de Technologie et d'Instrumentation in Grenoble, France. The accuracy of the scalar magnetic  
48 measurements was  $\pm 0.5$  nT and these magnetic field data was recorded every second (Rother  
49 et al. 2003).

50 *CHAMP* had a nearly circular, polar orbit its initial elevation of 456 km decreased due  
51 to upper atmospheric drag and it was boosted several times. The elevation interval of the orbit  
52 was between 319 and 340 km in 2008. The magnetic anomalies used in the present paper had  
53 been derived by the *NASA* by the application of the *CHAOS2* model (Olsen et al. 2009).

54

## 55 **2. Interpolation and coordinate transformation**

56

57 The aim of our calculations is the reduction and interpretation of the magnetic  
58 anomalies over the Pannonian Basin and its vicinity (latitude,  $38^\circ - 52^\circ$  North; longitude,  $14^\circ$   
59  $- 28^\circ$  East). The magnetic measurements are mapped on a spherical shell at 319–340 km  
60 elevation, and these data are given as a function of the latitude, longitude and elevation. The  
61 experimental frequencies of the latitude, longitude and elevation distributions of the recorded  
62 locations are plotted in Figure 1. As shown, they generally cover our study area. Data whose  
63 *Kp* index was less than or equal to 1 were selected for further processing. Using this criterion  
64 we obtained 107,927 data points. These data are interpolated into a spherical grid of  $0.5^\circ \times 0.5^\circ$   
65 at the elevation of 324 km.

66 The Gaussian weight function of the 3D interpolation is

67

$$68 \quad w(\Delta_i, k) = \frac{\pi^{3/2}}{k^3} \exp\left(-\frac{\pi^2}{k^2} \Delta_i^2\right), \quad (1)$$

69

70 where  $k$  is the parameter of the weight function,  $\Delta_i$  is the distance between the  $i$ th data  
71 observed and the single reference point of the spherical grid details are given by Véges  
72 (1971), Kis and Wittmann (1998), (2002). The interpolated value is normalized by the  
73 following:

74

75

$$T^{interpolated} = \frac{1}{\sum_{i=1}^n w_i} \sum_{i=1}^n T_i w_i, \quad (2)$$

76

77 where  $n$  is the number of data taken into consideration and  $T_i$  is the  $i$ th total magnetic anomaly  
 78 value. The interpolated total magnetic anomalies are plotted in Figure 2.

79 For the methods used in this study, the quantitative interpretation of the satellite  
 80 measured magnetic anomalies requires the transformation from a spherical to Cartesian  
 81 coordinates. The origin of the Cartesian coordinate system is  $\varphi = 47^\circ$  (latitude) and  $\lambda = 21^\circ$   
 82 (longitude) at an elevation of 324 km. In accordance with the general usage in geomagnetism,  
 83 the coordinate axes  $x$  and  $y$  directed towards the North and East, respectively, while the  $z$ -axis  
 84 points downwards. The details of these computations are given in the Appendix A.

85

### 86 3. Vertical derivative and downward continuation

87

88 Vertical gradient anomalies show good correlation with the probable extension of the  
 89 geologic body (Blakely 1995). They qualitatively delineate the lateral extension of the  
 90 magnetic source. The determination of the vertical gradients is a linear transform; its transfer  
 91 function is given by:

92

93

$$S(f_x, f_y) = 2\pi(f_x^2 + f_y^2)^{1/2}, \quad (3)$$

94

95 where  $f_x$  and  $f_y$  are the spatial frequencies in the  $x$  and  $y$  axes (Blakely, 1995). It has long been  
 96 recognized that high frequency amplification is undesirable, since these frequencies possess  
 97 the lowest signal-to-noise level. In order to eliminate noise this transfer function is multiplied  
 98 by a two-dimensional Gaussian low-pass window:

99

100

$$S_{LP}(f_x, f_y) = \exp(-k^2(f_x^2 + f_y^2)). \quad (4)$$

101

102 The parameter  $k$  controls the passed frequency range. The weight function of this transform  
 103 is:

104

105 
$$s(x, y) = \frac{\pi^{5/2}}{k^3} \exp\left(-\left(\frac{\pi^2(x^2 + y^2)}{k^2}\right)\right) M\left(-\frac{1}{2}, 1, \left(\frac{\pi^2(x^2 + y^2)}{k^2}\right)\right), \quad (5)$$

106

107 where M means the confluent hyper-geometric function. The details of this transform are  
 108 given by Kis and Pusztai (2006). The vertical gradients of the total magnetic anomalies at the  
 109 altitude of 324 km are plotted in Figure 3. A negative anomaly, with a minimum gradient of  
 110 0.01 nT/km, covers the Pannonian Basin. The spatial shape of the vertical gradient anomaly  
 111 determines the extension of our model in the inversion procedures.

112 The downward continuation of the magnetic anomalies can also be expressed as a  
 113 linear transform. Its transfer function is:

114

115 
$$S_{downward}(f_x, f_y) = \exp\left(2\pi h (f_x^2 + f_y^2)^{1/2}\right), \quad (6)$$

116

117 where  $h$  is the downward continuation value. Different authors (Bullard and Cooper, 1948; De  
 118 Meyer, 1974) have suggested the application of an appropriate window for the computation of  
 119 this transform. We used, however, Meskó (1984) for our procedure.

120

121 
$$\begin{aligned} S_{downward}(f_x, f_y) &= \exp\left(2\pi h (f_x^2 + f_y^2)^{1/2}\right) && \text{for } (f_x^2 + f_y^2)^{1/2} \leq f_{rc} \\ &= \exp\left(2\pi h (f_x^2 + f_y^2)^{1/2} - \gamma \left((f_x^2 + f_y^2)^{1/2} - f_{rc}\right)\right) && \text{for } (f_x^2 + f_y^2)^{1/2} > f_{rc}. \end{aligned} \quad (7)$$

122

123 This equation is our modified transfer function for the solution of the downward continuation.  
 124 From an earlier calculation we have the *CHAMP* total magnetic anomalies on the elevation of  
 125 425 km (Taylor et al. 2005). We will use this as our base level for the downward continuation.  
 126 This transformation is used for the downward continuation plotted in Figure 4. The  
 127 parameters of the downward continuation are: average sampling interval 41.3 km,  $h$  depth of  
 128 downward continuation. The appropriate value of the parameters of  $\gamma$  and  $f_{rc}$  is 145 and 0.005,  
 129 respectively. The anomalies at 425 and 324 km altitudes as well as the downward continued  
 130 anomalies are presented in Figure 4. The deviation between the calculated magnetic  
 131 anomalies and the downward continued anomalies is probably caused by the different depths  
 132 of the complex magnetic sources especially in the North-East part of the downwarded  
 133 anomalies, in the territory of the Carpathian Mts.

134

#### 4. Model of inversion and Bayesian inference

The magnetic anomaly map (324 km) reveals a large NW–SE oriented negative anomaly (-13 nT) in the middle of the Pannonian Basin (Figure 4). The qualitative interpretation of this anomaly was given by Taylor et al. (2005), the reverse magnetization of (-1.5 A/m) of the upper crust was the basis for their interpretation. The anomaly was forward modeled by a triangular polygonal prism using Plouff's (1976) method. Our calculated magnetic anomaly field (324 km) corresponds to the previous magnetic anomaly field (425 km) (Taylor et al. 2005).

The shape of the forward model and the magnetization are the same as they are in the qualitative interpretation (Taylor et al. 2005). For the solution of the inverse problem the magnetic anomaly of 324 km is used and the direction of the magnetization is  $\alpha = -60^\circ$ ,  $\beta = 60^\circ$ ,  $I = 60^\circ$  and  $D = 0^\circ$ , where  $\alpha$  and  $\beta$  are the inclination and declination of the magnetization and  $I$  and  $D$  are the inclination and declination of the Earth magnetic field. Model parameters are the top and bottom of the polygonal prism, and the three coordinate pairs of the horizontal triangle (Figure 5).

An effective tool of the geophysical inversion is the Bayesian inference. The mathematical basis and theory of the method are summarized, for example, by Box and Tiao (1973) and Tarantola (1987); its geophysical application is given by Duijndam (1988a), (1988b), Menke (1989), Sen and Stoffa (1995). The elements of the measured and model vectors are indicated by  $\mathbf{d}$  and  $\mathbf{m}$ ; they are random variables.

The conditional probabilities in the applied Bayesian equation (Bayes, 1763) is

$$p(\mathbf{m}|\mathbf{d})=p(\mathbf{d}|\mathbf{m})p(\mathbf{m}), \quad (8)$$

where  $p(\mathbf{m}|\mathbf{d})$  is the *a posteriori* conditional probability density,  $p(\mathbf{d}|\mathbf{m})$  is the likelihood conditional probability density, and  $p(\mathbf{m})$  is the *a priori* probability density.

The multivariate Gaussian *a posteriori* probability can be expressed as the multiplication of the *a priori* and likelihood probability densities. Disregarding the constant multipliers the *a posteriori* probability is given as:

$$p^{a\text{ posteriori}} \propto \exp\left(-\frac{1}{2}(\mathbf{m} - \mathbf{m}^{a\text{ priori}})^T \mathbf{C}_m^{-1} (\mathbf{m} - \mathbf{m}^{a\text{ priori}})\right).$$

166

$$\cdot \exp\left(-\frac{1}{2}(\mathbf{d}^{\text{measured}}(x, y) - T^{\text{calculated}}(x, y, \mathbf{m}))^T \mathbf{C}_D^{-1} (\mathbf{d}^{\text{measured}}(x, y) - T^{\text{calculated}}(x, y, \mathbf{m}))\right). \quad (9)$$

167

168 The  $\mathbf{m}^{a\text{ priori}}$  vector expresses the interpreter's decision to select the value of the model  
 169 parameters,  $\mathbf{C}_m$  is the *a priori* covariance matrix superscript  $T$  indicates the transpose vectors.  
 170 The variances in the matrix  $\mathbf{C}_m$  express the uncertainty of the interpreter.  $T^{\text{calculated}}(x, y, \mathbf{m})$   
 171 represents the calculated magnetic direct problem with the parameters  $\mathbf{m}$  at the  $x, y$   
 172 coordinates.  $\mathbf{C}_D$  is the data covariance matrix. It consists of two parts (1) the measurements  
 173 uncertainty matrix  $\mathbf{C}_d$  (the measurements variances), and (2) the model error matrix  $\mathbf{C}_T$ ,  
 174 namely

175

$$\mathbf{C}_D = \mathbf{C}_d + \mathbf{C}_T. \quad (10)$$

177

178 The elements of the model error matrix are also determined by the interpreter. This matrix  
 179 contains the goodness of the selected model.

180 The model parameter values of the source can be determined by the solution of an  
 181 optimum problem. It means maximizing the *a posteriori* probability density as a function of  
 182  $\mathbf{m}$ . This is equivalent to minimizing the sum of exponents of the Equation (9). The objective  
 183 function  $E(\mathbf{m})$  has the following form of

184

$$E(\mathbf{m}) = \left( (\mathbf{m} - \mathbf{m}^{a\text{ priori}})^T \mathbf{C}_m^{-1} (\mathbf{m} - \mathbf{m}^{a\text{ priori}}) \right) + \\ + \left( (\mathbf{d}^{\text{measured}}(x, y) - T^{\text{calculated}}(x, y, \mathbf{m}))^T \mathbf{C}_D^{-1} (\mathbf{d}^{\text{measured}}(x, y) - T^{\text{calculated}}(x, y, \mathbf{m})) \right). \quad (11)$$

186

187 The minimum of the objective function is determined by a numerical method.

188 The last step of the interpretation is the calculation of the *a posteriori* covariance  
 189 matrix  $\mathbf{C}'_m$ . It is given in the form

190

$$\mathbf{C}'_m \approx (\mathbf{G}_n^T \mathbf{C}_D^{-1} \mathbf{G}_n + \mathbf{C}_m^{-1})^{-1} \quad (12)$$

192

193 (Tarantola, 1987) and  $\mathbf{G}_n$  is given by

194

$$195 \quad \mathbf{G}_n = \left( \frac{\partial T}{\partial \mathbf{m}} \right)_{\mathbf{m}=\mathbf{m}_n} . \quad (13)$$

196

197 The multivariate Laplace *a posteriori* probability density distribution is given by the  
198 following:

199

$$200 \quad p^{a\text{ posteriori}} \propto \exp\left(-\frac{|\mathbf{m} - \mathbf{m}^{a\text{ priori}}|}{\mathbf{C}_m^{1/2}}\right) \cdot \exp\left(-\frac{|\mathbf{d}^{\text{measured}}(x, y) - T^{\text{calculated}}(x, y, \mathbf{m})|}{\mathbf{C}_D^{1/2}}\right), \quad (14)$$

201

202 where we disregard the constant multipliers. The objective function is expressed by the  
203 equation:

204

$$205 \quad E(\mathbf{m}) = \left( \frac{|\mathbf{m} - \mathbf{m}^{a\text{ priori}}|}{\mathbf{C}_m^{1/2}} \right) + \left( \frac{|\mathbf{d}^{\text{measured}}(x, y) - T^{\text{calculated}}(x, y, \mathbf{m})|}{\mathbf{C}_D^{1/2}} \right). \quad (15)$$

206

207 The minimum problem is solved by the Simplex (Walsh, 1975) and Simulated  
208 annealing (Kirkpatrick et al. 1983, Sen and Soffa 1995) methods. The minimum problems are  
209 solved by  $L_2$  norm in the case of the Gaussian probability and by  $L_1$  norm in the case of the  
210 Laplace probability. Figures 6 and 7 show the objective functions *versus* iterative steps. These  
211 figures illustrate how these two optimum procedures work. The parameters estimated by the  
212 former numerical methods are summarized in Table 1. The covariance matrices are diagonal;  
213 there are no correlations between the related parameters. The *a priori* variances are set to  $(5$   
214  $\text{nT})^2$ , variances of the measured data are set to  $(0.5 \text{ nT})^2$ . Because the complex structure of the  
215 direct problem the elements of the *a posteriori* covariance matrix are approximated by  
216 difference quotients of Equation (13).

217

218 Figure 8 shows those residual anomalies that determine the application of the  
219 parameters given in Table 1. The residuals in the four parts of the figure are calculated for  
220 Gaussian and Laplace parameter distributions determined by Simplex and Simulated  
221 annealing methods. It can be concluded that the lowest residuals are given by the Laplace  
222 distribution parameters obtained by the Simulated annealing method.

222

223 **5. Possible origin of the magnetization of sources**

224

225 Large amplitude magnetic anomalies have been mapped by aircraft and satellites over  
226 regions of the Earth and by satellite over the Martian crust. Many of these anomalies have  
227 negative signs. For our geological interpretation we call upon analogous source regions such  
228 as the Mid-Proterozoic granulites in southwestern Sweden (McEnroe et al. 2001); Proterozoic  
229 Åna Sira anorthosite in Rogaland, Norway (Robinson et al. 2002, McEnroe et al. 2004, 2005)  
230 and the metamorphic complex in Modum district, Southern Norway (Fabian et al. 2008).

231 The magnetic properties of these rocks have been investigated by the above mentioned  
232 authors. They suggest that the stable remanent magnetization is caused by the exsolution of  
233 the hematite-ilmenite minerals. This exsolution can produce stable ferrimagnetism which is  
234 investigated by model calculation (Robinson et al. 2002) and transmission electron  
235 microscopy analysis (McEnroe et al. 2005). These analyses show 1  $\mu\text{m}$  to 4 nm exsolution of  
236 both hematite lamella in ilmenite hosts and ilmenite lamella in hematite hosts. The contact  
237 zone of these minerals can produce strong ferromagnetic effect which belongs to neither  
238 hematite nor ilmenite source rocks.

239 According to Kleteschka et al. (2002) stable remanent magnetization can be developed  
240 in the hemo-ilmenite minerals. The remanent magnetization is formed in the cooling process.  
241 The anti-ferromagnetic hemo-ilmenite lamellas have multi-domain structures. They are able  
242 to form intense thermo-remanent magnetization. This process can be more intensive in the  
243 exsolution of hematite-ilmenite minerals.

244 Is this kind of magnetization found in the crust of the Pannonian Basin? The deep  
245 magnetic sources are located in the upper crust; they probably belong to the eastern part of  
246 Variscan Europe (Szederkényi 1996, Tari and Pamić 1998). The granulite xenoliths and  
247 peridotite xenoliths obtained from the Pliocene basaltic rocks located in the Balaton  
248 Highlands (Pelso-unit, part of the African Alcapa block). These granulite and peridotite  
249 xenoliths discovered in these locations show crustal and upper mantle origins as suggested by  
250 Embey-Isztin et al. (2003) and Dobosi et al. (2003). According to the thermo-barometric  
251 investigations of these xenoliths they formed at a temperature of 800–900° C and at pressures  
252 of 8–15 kbar (0.8 to 15 GPa). These meta-volcanic xenoliths have apparently formed at a  
253 depth of 40–50 km. This depth is significantly deeper than the present 25–30 km thick crust.  
254 The present crust was developed in the Tertiary due to the NW–SE extension of the  
255 Pannonian Basin (Konečný et al. 2002). The alkaline basaltic rocks were formed in the

256 Pliocene after the intense widespread Miocene calc-alkaline volcanism (Embey-Isztin et al.  
257 2001).

258 The international literature discusses a few other possible solutions for source of large  
259 negative magnetic anomalies. Due to the unknown parameters of the source rock in the upper  
260 crust like age or direction of its magnetization, as well as accurate composition of this rock  
261 we can not propose proven fact for the source. But the granulite xenoliths and peridotite  
262 xenoliths obtained from the Pliocene basaltic rocks located in the Pannonian Basin give light  
263 evidence of the significant part of the negative anomaly presented in this study is derived to  
264 the exsolution of hematite-ilmenite minerals.

265

266

## 267 **6 Conclusions**

268

269 The total magnetic field, vertical gradient and downward continued anomalies indicate  
270 a magnetic low over the Pannonian Basin. Our inversion method determined that the source  
271 region was in the upper crust of the basin. We propose that the strong magnetization can be  
272 produced in the crust of the Pannonian Basin. The *CHAMP* magnetic anomaly can be  
273 explained by the exsolution of hemo-ilmenite minerals. It has been previously reported that  
274 hematite-ilmenite mineralogy can produce stable remanent magnetization in the crust and in  
275 our study we propose that the crustal rocks of the Pannonian Basin display negative remanent  
276 magnetization. We further propose that some of the magnetic source bodies were formed  
277 during the late Miocene-Pliocene tectonic activity of compression and extension and/or  
278 volcanism (Hámor, 2001) and emplaced in the upper crust.

279

## 280 **Appendix A**

281

282 It is often required the transform of the satellite data from the spherical polar  
283 coordinates to Cartesian *xyz* coordinate system. This transformation can be done in two steps:  
284 one translation and rotation.

285 The origin of the *XYZ* coordinate system is in the center of the Earth. The *X*-axis is in  
286 the plane of the equator and points to the Greenwich meridian. The *Z*-axis coincides with the  
287 Earth's rotation axis and points upward. The *Y*-axis is also in the plane of the equator and  
288 perpendicular to the *XZ* sheet and points to East. The *X*, *Y*, and *Z* coordinates of the satellite  
289 data are:

290

291 
$$X=r \sin \theta \cos \lambda , \quad Y=r \sin \theta \sin \lambda , \quad Z=r \cos \theta , \quad (\text{A.1})$$

292

293 where  $r$  is the distance from the center of the Earth,  $\theta$  and  $\lambda$  are the colatitude and longitude,  
294 respectively.

295 Let us translate the origin of the  $x'y'z'$  Cartesian coordinate system in the central  
296 point  $(r_0, \theta_0, \lambda_0)$ , where  $r_0 = \text{Earth's radius} + \text{altitude of the satellite}$ . The  $x'$ ,  $y'$ , and  $z'$  axes are  
297 parallel to the  $X, Y$ , and  $Z$  axes. The  $t_x, t_y$ , and  $t_z$  coordinates of this point in the  $XYZ$  coordinate  
298 system are

299

300 
$$t_x=r_0 \sin \theta_0 \cos \lambda_0 , \quad t_y=r_0 \sin \theta_0 \sin \lambda_0 , \quad t_z=r_0 \cos \theta_0 . \quad (\text{A.2})$$

301

302 The equations of translation are:

303

304 
$$x'=X-t_x , \quad y'=Y-t_y , \quad z'=Z-t_z . \quad (\text{A.3})$$

305

306 The origin of the rotated Cartesian  $xyz$  coordinate system is the point  $(r_0, \theta_0, \lambda_0)$ , where  
307 the  $x$ -axis points to the geographic North; the  $y$ -axis to the East; and the  $z$ -axis points  
308 downward. The equations of rotation are:

309

$$x=-x' \cos \theta_0 \cos \lambda_0 -y' \cos \theta_0 \sin \lambda_0 +z' \sin \theta_0$$

310

$$y=-x' \sin \lambda_0 -y' \cos \lambda_0 \quad (\text{A.4})$$

$$z=-x' \sin \theta_0 \cos \lambda_0 -y' \sin \theta_0 \sin \lambda_0 +z' \cos \theta_0 .$$

311

312 **Acknowledgement**

313

314 Dr. Michael Purucker (Raytheon STX Corporation, NASA/GSFC) aided in obtaining these  
315 data which were kindly provided by the GFZ, POTSDAM, GERMANY. Mr. Terry J. Sabaka  
316 and Dr. Paul D. Lowman Jr. (NASA/GSFC) pre-reviewed our manuscript and made  
317 constructive comments.

318

319 **References**

320

321 Bayes, T., 1773. An essay towards solving a problem in the doctrine of chances, *Phil. Trans.*  
322 *Roy. Soc.* 53, 370–418 (republished in *Biometrika*, 45 (1958) 293–315).

323 Blakely, R. J., 1995. *Potential Theory in Gravity and Magnetic Applications*, Cambridge  
324 University Press.

325 Box, G. E. P., Tiao, G. C., 1973. *Bayesian Inference in Statistical Analysis*, Addison-Wesley  
326 Publishing Company, London, Don Mills, Reading, Menlo Park.

327 Bullard, E. C., Cooper, R. I. B., 1948. Determination of the masses necessary to produce a  
328 given gravitational field, *Proc. Roy. Soc. of London, A* 194, 332–347.

329 De Meyer, F., 1974. Filter techniques in gravity interpretation, *Adv. Geophys.* 17, 187–261.

330 Dobosi, G., Kempton, P. D., Downes, H., Embey-Isztin, A., Thirlwall, M., Greenwood, P.,  
331 2003. Lower crustal granulite xenoliths from the Pannonian Basin, Hungary, Part 2: Sr-Nd-  
332 Pb-Hf and O isotope evidence for formation of continental lower crust by tectonic  
333 emplacement of oceanic crust, *Contrib. Mineral. Petrol.* 144, 671–683.

334 Duijndam, A. J. W., 1988a. Bayesian estimation in seismic inversion. Part I: Principles,  
335 *Geophys. Prosp.* 36, 899–918.

336 Duijndam, A. J. W., 1988b. Bayesian estimation in seismic inversion. Part II: Uncertainty  
337 analysis, *Geophys. Prosp.* 36, 878–898.

338 Embey-Isztin, A., Dobosi, G., Altherr, R., Meyer, H-P., 2001. Thermal evolution of the  
339 lithosphere beneath the western Pannonian Basin: evidence from deep-seated xenoliths,  
340 *Tectonophysics* 331, 283–305.

341 Embey-Isztin, A., Downes, H., Kempton, P. D., Dobosi, G., Thirlwall, M., 2003. Lower  
342 crustal granulite xenoliths from the Pannonian Basin, Hungary. Part 1: mineral chemistry,  
343 thermobarometry and petrology, *Contrib. Mineral. Petrol.* 144, 652–670.

344 Fabian, K., McEnroe, S. A., Robinson, P., Shcherbakov, V. P., 2008. Exchange bias  
345 identifies lamellar magnetism as the origin of the natural remanent magnetization in  
346 titanohematite with ilmenite exsolution from Modum, Norway, *Earth Planet. Sci. Lett.* 268,  
347 339–353.

348 Hámor, G., 2001. Genesis and evolution of the Pannonian Basin, in: J. Haas (Ed), *Geology of*  
349 *Hungary*, Eötvös University Press, Budapest, 193–242.

350 Kirkpatrick, S., Gelatt Jr. C. D., Vecchi, M. P., 1983. Optimization by simulated annealing,  
351 *Science* 220, 671–680.

352 Kis, K. I., Pusztai, S., 2006. Application of the magnetic field derivatives for locating  
353 Sarmatian graves, *J. Appl. Geophys.* 60, 13–26.

354 Kis, K. I., Wittmann, G., 1998. Determination of vertical magnetic anomalies and equivalent  
355 layer for the European region from the Magsat measurements, *J. Appl. Geophys.* 39, 11–24.

356 Kis, K. I., Wittmann, G., 2002. 3D reduction of satellite magnetic measurements to obtain  
357 magnetic anomaly coverage over Europe, *J. Geodyn.* 33, 117–129.

358 Konečný, V., Kovač, M., Lexa, J., Šefara, J., 2002. Neogene evolution of the Carpatho-  
359 Pannonian region: an interplay of subduction and back-arc diapiric apprise in the mantle,  
360 EGU Stephan Mueller Special Publication Series I, 105–123.

361 Kletetschka, G., Wasilewski, P. J., Taylor, P. T., 2002. The role of hematite–ilmenite solid  
362 solution in the production of magnetic anomalies in ground and satellite-based data,  
363 *Tectonophysics*, 347, 166–177.

364 McEnroe, S. A., Harrison, R. J., Robinson, P., Golla, U., Jercinovic, M. J., 2001. Effect of  
365 fine-scale microstructures in titanohematite on the acquisition and stability of natural  
366 remanent magnetization in the granulite facies metamorphic rocks, southwest Sweden:  
367 Implications for crustal magnetism, *J. Geophys. Res.*, 106 B12, 30,523–30,546.

368 McEnroe, S. A., Langenhorst, F., Robinson, P., Bromiley, G. D., Shaw, C. S. J., 2004. What  
369 is magnetic in the lower crust? *Earth Planet. Sci. Lett.* 226, 175–192.

370 McEnroe, S. A., Harrison, R. J., Jackson, M. J., Hirt, A. M., Robinson, P., Langenhorst, F.,  
371 Heidelbach, F., Kasama, T., Putnis, A., Brown, L. L., Golla-Schindler, U., 2005. Lamellar  
372 magnetism: Effects of interface versus exchange interactions of nanoscale exsolutions in  
373 ilmenite-hematite system, *J. Phys. Conference Series*, 17, 154–167.

374 Menke, W., 1989. *Geophysical Data Analysis: Discrete Inverse Theory*, Academic Press, Inc.  
375 San Diego, New York, Boston, Sydney, Tokyo, Toronto.

376 Meskó, A., 1984. *Digital Filtering: Applications in Geophysical Exploration for Oil*,  
377 Akadémiai Kiadó, Budapest.

378 Olsen, N., Manda, M., Sabaka, T. J., Tøffner-Clasen, L., 2009. *CHAOS-2* a geomagnetic  
379 field model derived from one decade of continuous satellite data, *Geophys. J. Int.*, 179, 1477–  
380 1487.

381 Plouff, D., 1976. Gravity and magnetic fields of polygonal prism and application to magnetic  
382 terrain corrections, *Geophysics* 41, 727–741.

383 Reigber, C., Lühr, H., Schwintzer, P., (Eds.), 2003. *First CHAMP Mission Results for*  
384 *Gravity, Magnetism and Atmospheric Studies*, Springer-Verlag, Berlin.

385 Reigber, C., Lühr, H., Schwintzer, P., Wickert, J., (Eds), 2005. *Earth Observations with*  
386 *CHAMP Results from Three Years in Orbit*. Springer-Verlag, Berlin.

- 387 Robinson, P., Harrison, R. J., McEnroe, S. A., Hargraves, R. B., 2002. Lamellar magnetism  
388 in the hematite–ilmenite series as an explanation for strong remanent magnetization, *Nature*,  
389 418, 517–520.
- 390 Rother, M., Choi, S., Lühr, H., Mai, W., 2003. CHAMP ME data Processing and Open Issues,  
391 in: C. Reigber, H. Lühr, P. Schwintzer, P. (Eds.), *First CHAMP Mission Results For Gravity,*  
392 *Magnetics and Atmospheric Studies*, Springer-Verlag, Berlin.
- 393 Sen, M., Stoffa, P. L., 1995. *Global Optimization Methods in Geophysical Inversion*,  
394 Elsevier, Amsterdam, Lausanne, New York, Oxford, Shannon, Tokyo.
- 395 Szederkényi, T., 1996. Metamorphic formations and their correlation in the Hungarian part of  
396 the Tisia Megaunit (Tisia Composite Terrane), *Acta Mineralogica-Petrographica*. Szeged, 37,  
397 143–160.
- 398 Tarantola, A., 1987. *Inverse Problem Theory*, Elsevier, Amsterdam, Oxford, New York,  
399 Tokyo.
- 400 Tari, V., Pamić, J., 1998. Geodynamic evolution of the northern Dinarides and southern part  
401 of the Pannonian Basin, *Tectonophysics* 297, 269–281.
- 402 Taylor, P. T., Kis, K. I., von Frese, R. R. B., Korhonen, J. V., Wittmann, G., Kim, H. R.,  
403 Potts, L. V., 2005. Effects of varying crustal thickness on CHAMP geopotential data, in:  
404 Reigber, Ch., H. Lühr, J. Schwintzer, (Eds.), *Earth Observation with CHAMP*, Springer-  
405 Verlag, Berlin, Heidelberg, New York, 279–286.
- 406 Véges, I., 1971. Map plotting with weighted average on the surface of a circular disc, *Pure*  
407 *Appl. Geophys.* 78, 5–17.
- 408 Walsh, G. R., 1975. *Methods of Optimization*, John Willey & Sons, London, New York,  
409 Sydney, Toronto.

410

#### 411 **Captions**

412

413 Figure 1. Experimental frequency of the *CHAMP* magnetic anomalies *versus* latitude,  
414 longitude and altitude over the Pannonian Basin and vicinity.

415

416 Figure 2. The *CHAMP* total magnetic anomaly map determined by interpolation of data from  
417 the Pannonian Basin region, plotted on an Albers' projection at 324 km altitude; anomalies  
418 are in nT with a range of 22 grey levels and a contour interval of 1 nT, inner frame shows the  
419 investigated territory.

420

421 Figure 3. The vertical gradient map of the *CHAMP* total magnetic anomaly field, plotted in  
422 Albers' projection at the altitude of 324 km; anomalies in nT/km with a 14 grey scale levels  
423 and a contour interval of 0.005 nT/km, inner frame shows the investigated territory.

424

425 Figure 4. *CHAMP* magnetic anomaly maps at (a) 425 km and (b) 324 km altitude; (c)  
426 downward continued magnetic anomaly map from 425 km to 324 km, the maps are plotted on  
427 Albers' projection; grey scale units in nT.

428

429 Figure 5. Three dimensional triangular model of the magnetic source body we used in the  
430 inverse problem, upper and lower depths are indicated by:  $z_T$  and  $z_B$ , respectively, the  
431 triangular base is given by three coordinate pairs:  $(x_1, y_1)$ ,  $(x_2, y_2)$  and  $(x_3, y_3)$ .

432

433 Figure 6. Logarithm of the objective functions determined by Simplex method *versus* iterative  
434 steps in the case of the Gaussian and Laplace distribution model parameters.

435

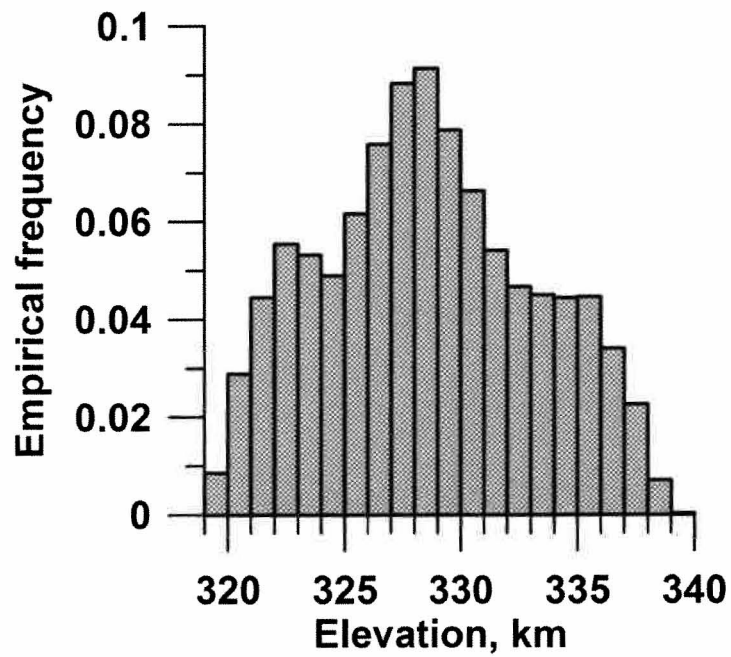
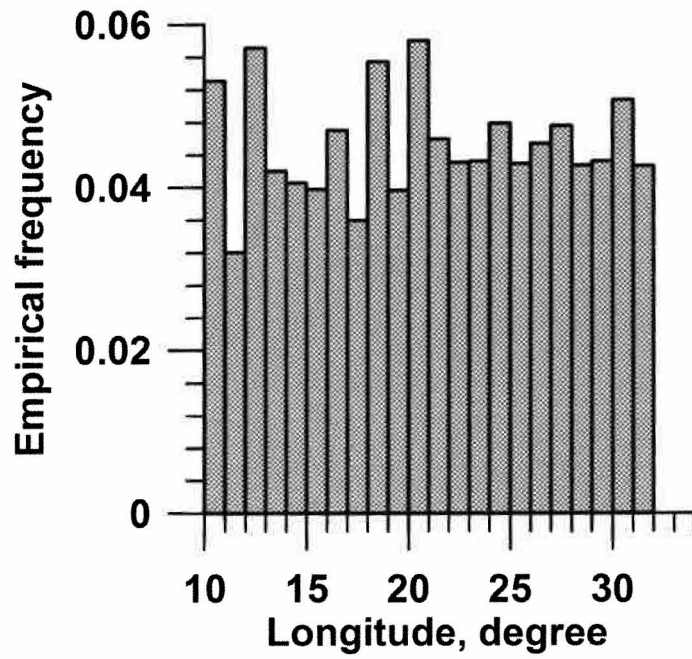
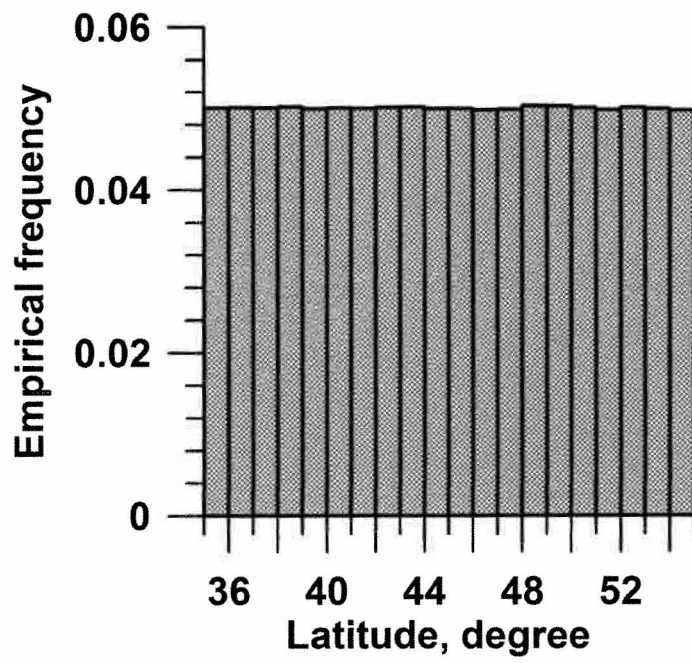
436 Figure 7. Logarithm of the objective functions determined by Simulated annealing method  
437 *versus* iterative steps in the case of the Gaussian and Laplace distribution model parameters.

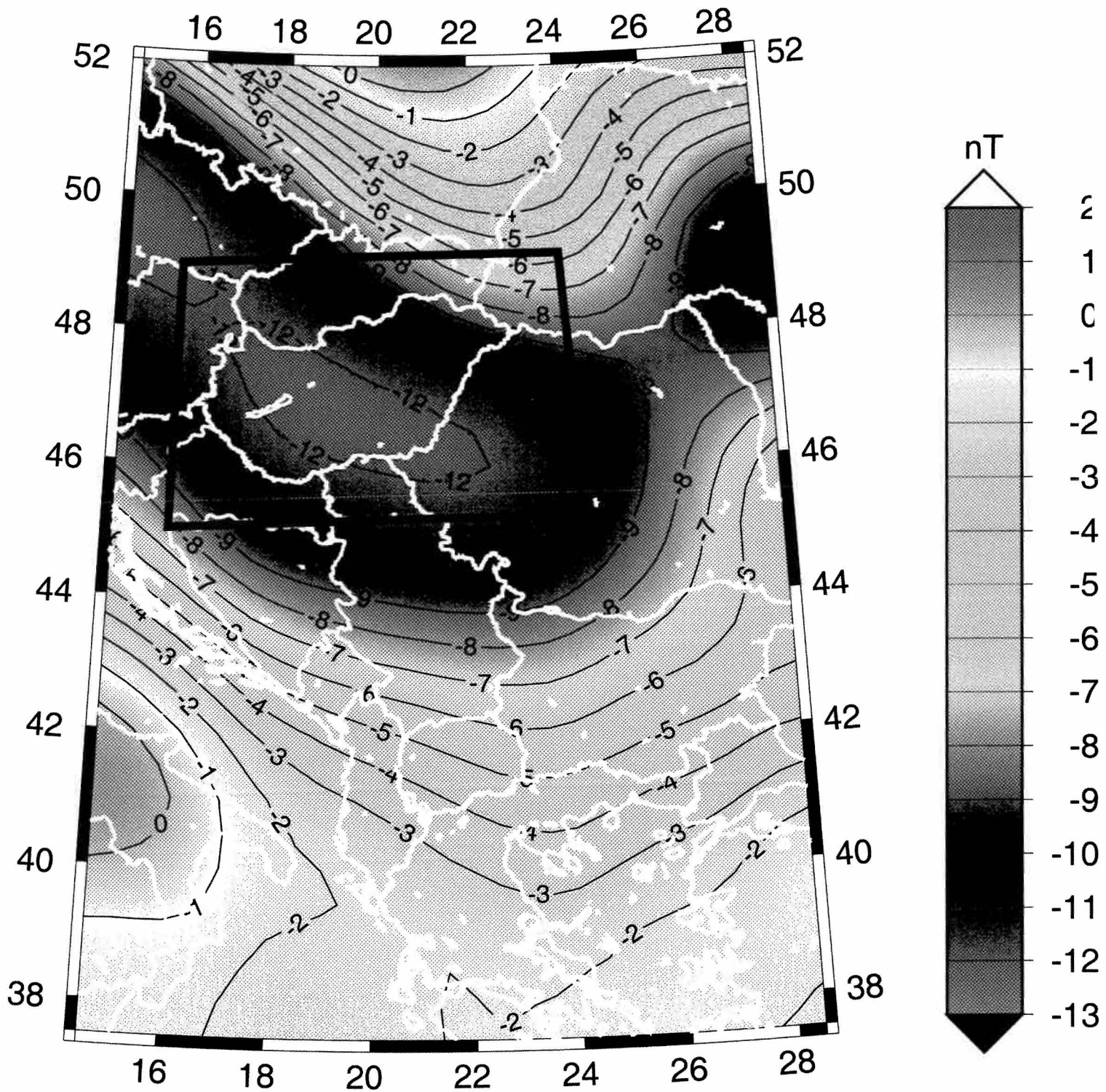
438

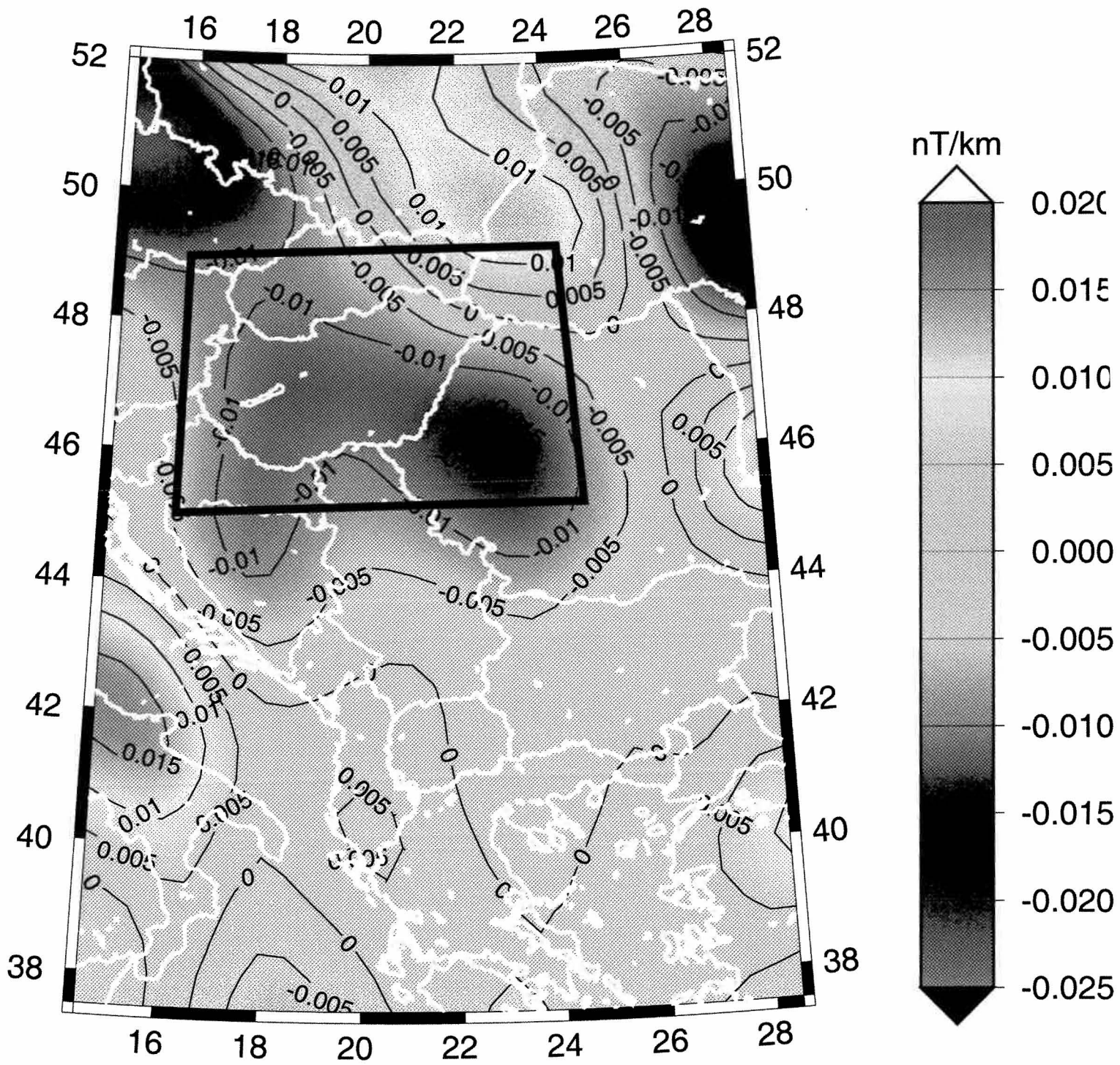
439 Figure 8. Residual anomalies in the case of the Gauss and Laplace distributed model  
440 parameters when the minimum problem is solved by Simplex and Simulated annealing  
441 methods; anomalies are in nT unit in a gray scale, horizontal coordinates are given in km.

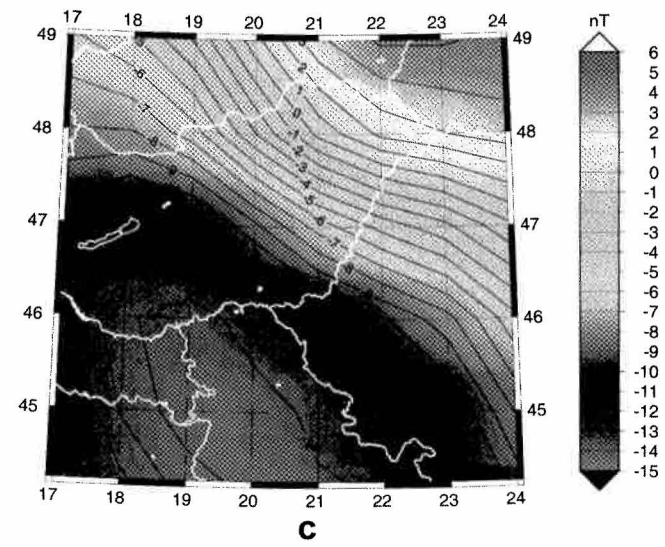
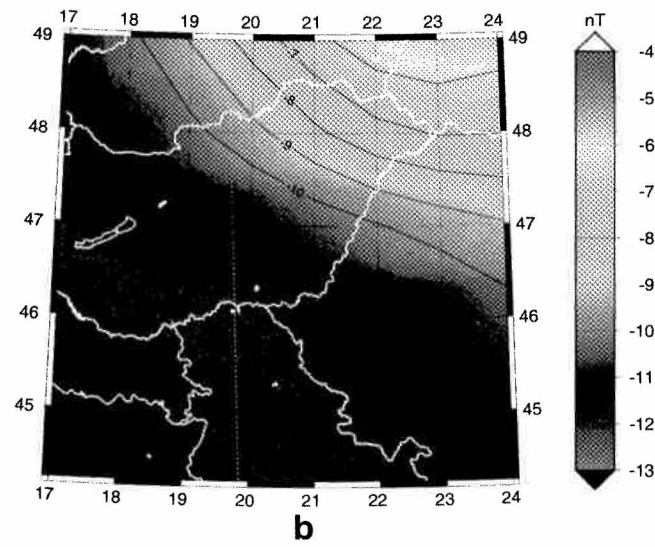
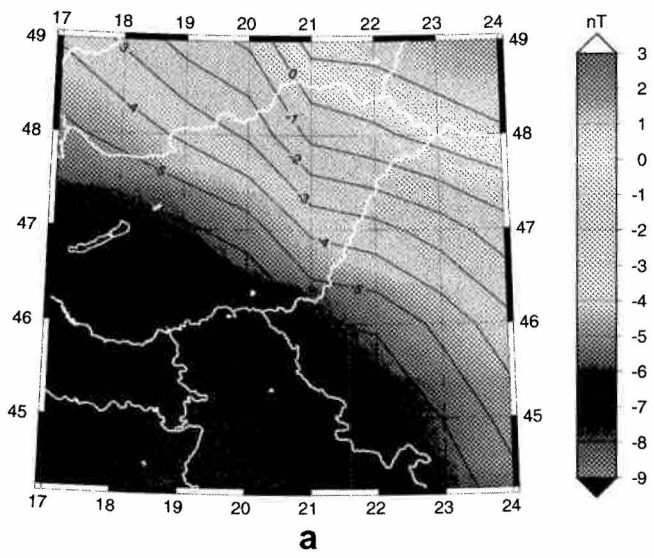
442

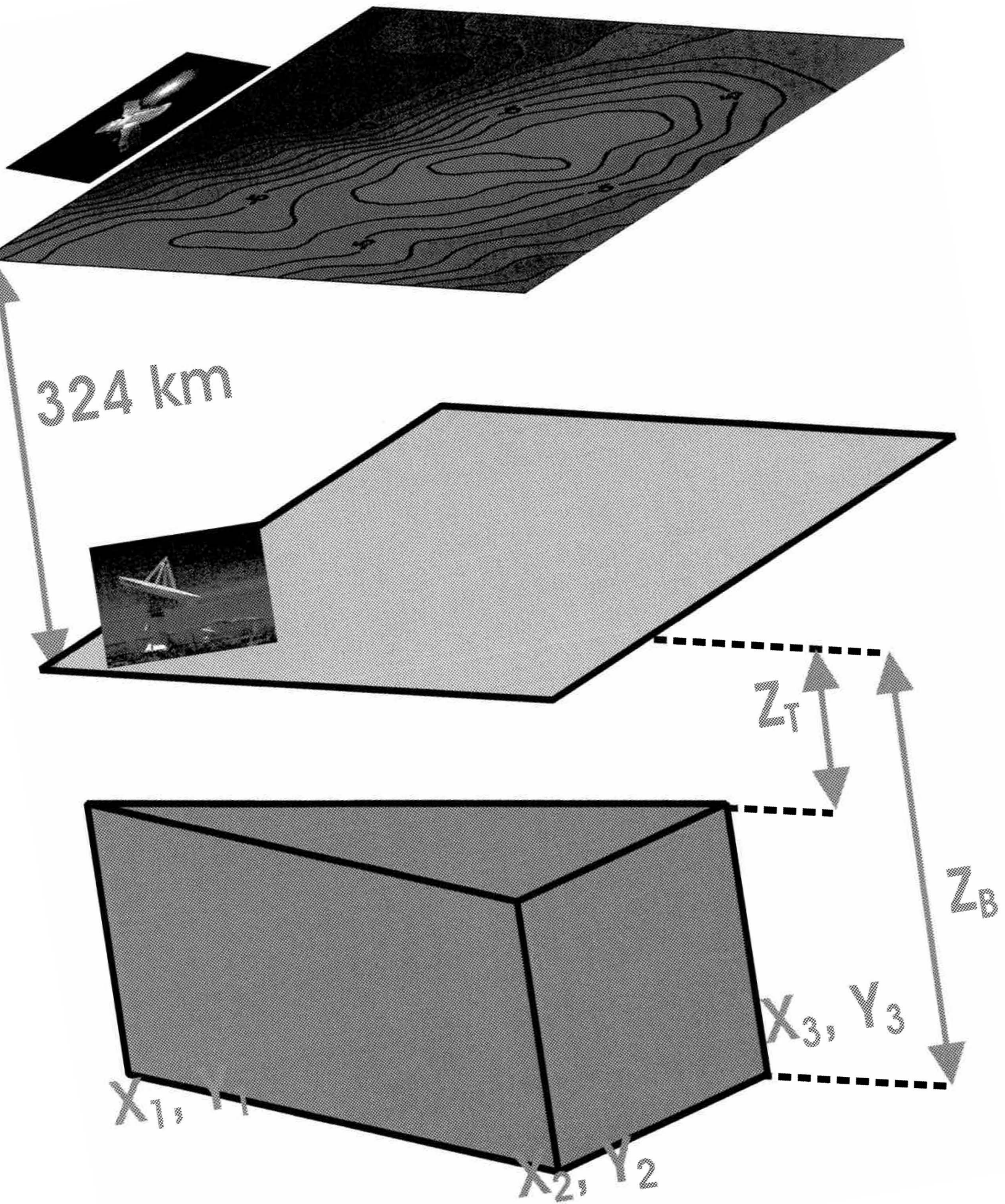
443 Table 1. Determined parameters by Simplex and Simulated annealing methods in the case of  
444 the Gaussian and Laplace parameter distributions.



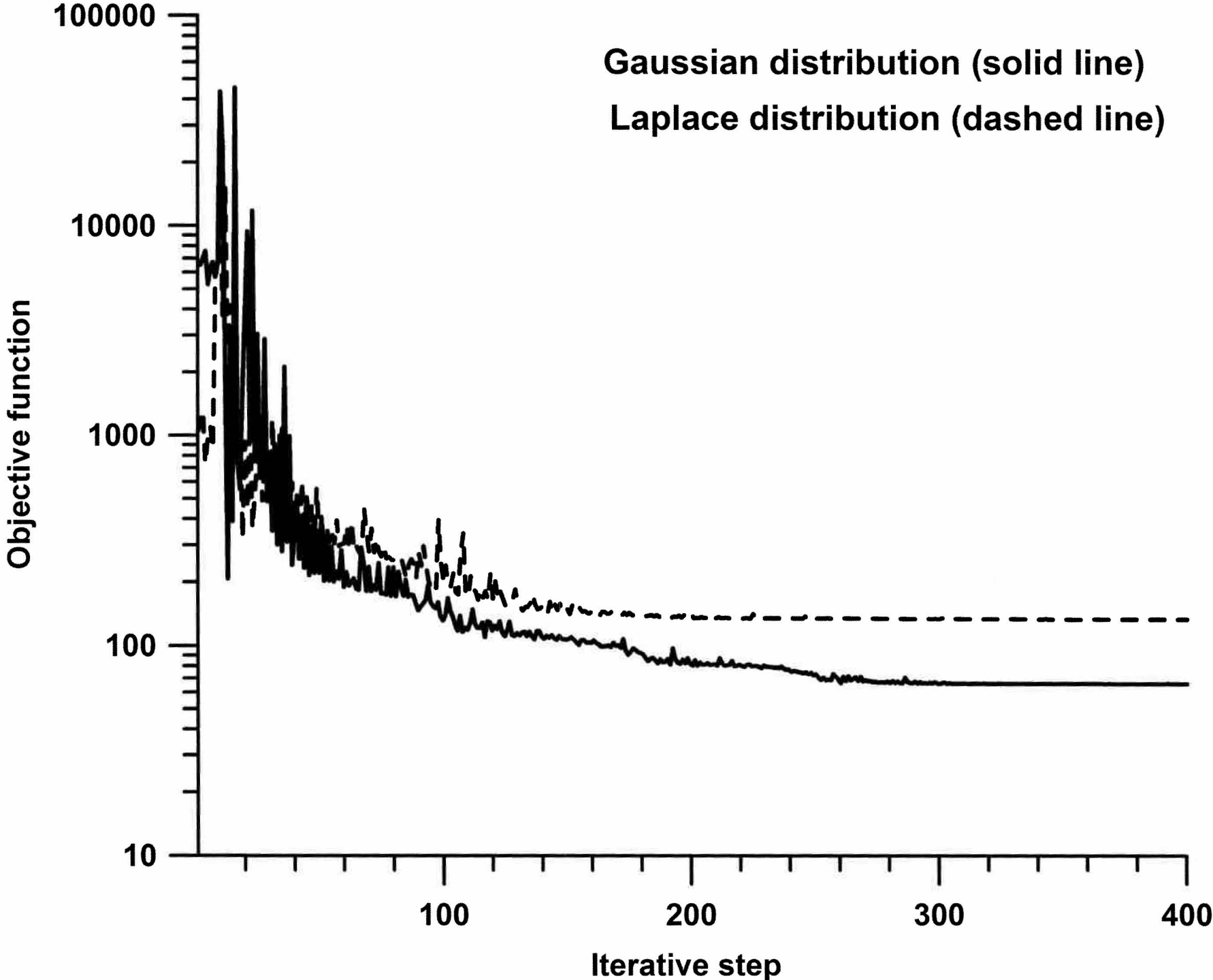








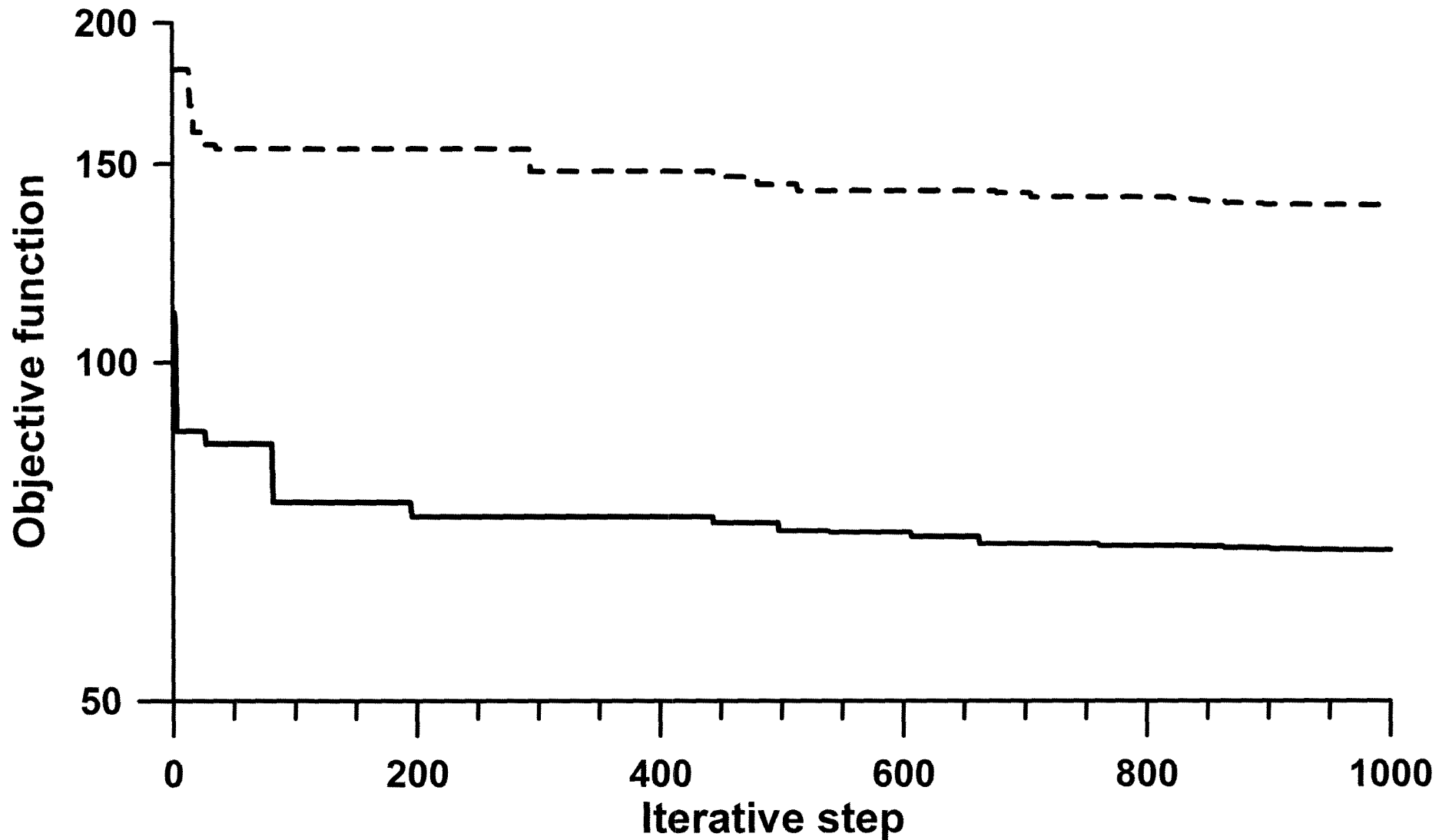
# Simplex method



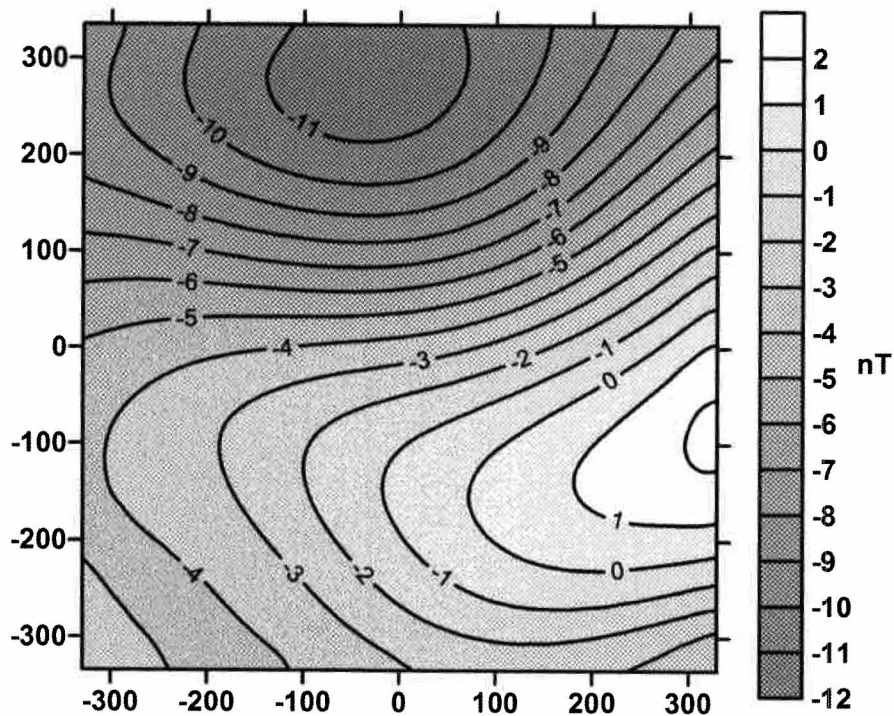
# Simulated annealing method

Gaussian distribution (solid line)

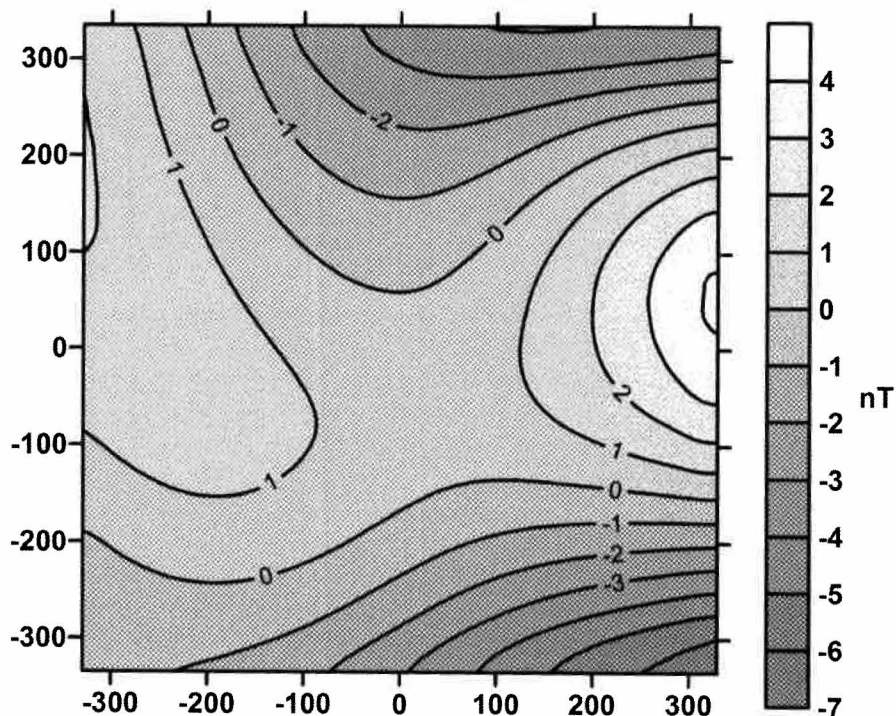
Laplace distribution (dashed line)



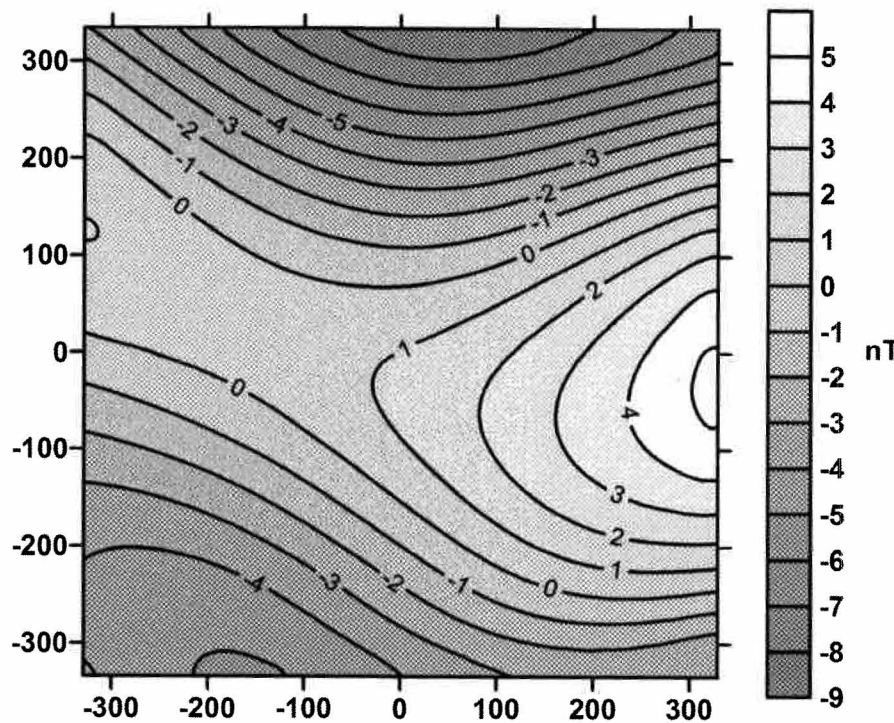
Gaussian distribution, Simplex method



Laplace distribution, Simplex method



Gaussian distribution, Simulated annealing method



Laplace distribution, Simulated annealing method

